Research Article

Nano Research
2021, 14(11): 4220–4226

ISSN 1998-0124 CN 11-5974/O4
https://doi.org/10.1007/s12274-021-3531-8

Construction of hierarchical $FeNi_3$@(Fe,Ni)S_2 core–shell heterojunctions for advanced oxygen evolution

Minglei Yan[1], Zhiyang Zhao[1], Peixin Cui[2], Kun Mao[1], Chi Chen[3], Xizhang Wang[1], Qiang Wu[1], Hui Yang[3], Lijun Yang[1] (✉), and Zheng Hu[1] (✉)

[1] *Key Laboratory of Mesoscopic Chemistry of MOE and Jiangsu Provincial Laboratory of Nanotechnology, School of Chemistry and Chemical Engineering, Nanjing University, Nanjing 210023, China*
[2] *Key Laboratory of Soil Environment and Pollution Remediation, Institute of Soil Science, Chinese Academy of Sciences, Nanjing 210008, China*
[3] *Shanghai Advanced Research Institute, Chinese Academy of Sciences, Shanghai 201210, China*

Received: 6 March 2021 / **Revised:** 15 April 2021 / **Accepted:** 19 April 2021

ABSTRACT

The investigation of earth-abundant electrocatalysts for efficient water electrolysis is of central importance in renewable energy system, which is currently impeded by the large overpotential of oxygen evolution reaction (OER). NiFe sulfides show promising OER activity but are troubled by their low intrinsic conductivities. Herein, we demonstrate the construction of the porous core–shell heterojunctions of $FeNi_3$@(Fe,Ni)S_2 with tunable shell thickness via the reduction of hierarchical $NiFe(OH)_x$ nanosheets followed by a partial sulfidization. The conductive $FeNi_3$ core provides the highway for electron transport, and the (Fe,Ni)S_2 shell offers the exposed surface for *in situ* generation of S-doped NiFe-oxyhydroxides with high intrinsic OER activity, which is supported by the combined experimental and theoretical studies. In addition, the porous hierarchical morphology favors the electrolyte access and O_2 liberation. Consequently, the optimized catalyst achieves an excellent OER performance with a low overpotential of 288 mV at 100 mA·cm^{-2}, a small Tafel slope of 48 mV·dec^{-1}, and a high OER durability for at least 1,200 h at 200 mA·cm^{-2}. This study provides an effective way to explore the advanced earth-abundant OER electrocatalysts by constructing the heterojunctions between metal and corresponding metal-compounds via the convenient post treatment, such as nitridation and sulfidization.

KEYWORDS

oxygen evolution reaction, electrocatalysts, Ni-Fe nitrides, core–shell structure, heterojunctions

1 Introduction

The renewable energies, such as solar, wind, tidal and geothermal resources, are attracting increasing worldwide interests, but they have the limitation of intermittency [1, 2]. Hydrogen gas (H_2) is a clean, carbon-neutral, and high-energy carrier to make the renewable energy stable and redistributable [3, 4], which can be achieved through electrochemical water splitting but currently impeded by the sluggish kinetics of oxygen evolution reaction (OER) due to the complicated four-step electron transfer process [5–8]. The high-performance OER electrocatalysts are essential to the efficient hydrogen production. Currently, the benchmark OER electrocatalysts are IrO_2 and RuO_2, but the high price and scarce resources limit their wide application, which stimulates the exploration of non-precious metal-based alternatives [8–11]. Among the various candidates, the NiFe-based compounds usually exhibit high activity in alkaline electrolytes [5, 12], which could trace back to 100 years ago [13]. Recent *in situ* characterizations and theoretical calculations reveal that the NiFe-based compounds are actually the pre-catalysts, and the *in situ* formed surface NiFe-oxyhydroxides are the real active species of OER [14, 15]. The edge atoms of the layered NiFe-oxyhydroxides are identified as the active sites, in which the Fe site delivers the O radical and Ni site catalyzes the O–O coupling during OER [16]. The OER performance is mainly determined by: 1) the intrinsic activity of the active sites, and 2) the electric resistance along the pathway from the active sites to current collector. More and more results indicate that the NiFe derivatives, such as nitrides [17], sulfides [18], and phosphides [19] have higher activity than the corresponding oxides and hydroxides, which might be associated with the formation of heteroatoms-doped oxyhydroxides during OER with more suitable adsorption for OER intermediates. The very recent study on N- and Se-containing catalysts confirmed the formation of N- or Se-doped oxyhydroxides with modified electronic structures [20–22]. As known, the NiFe-based compounds usually have low conductivity, hence should be deposited on the conductive substrate or constructed into nano-sized architectures to ensure facile electron transport [23–25], which brings the issues of complicated process, unsatisfactory electronic interaction, and low loading amount. Our recent study indicated that the heterojunctions of metal/metal-nitride constructed by post nitridation can form the atomic epitaxial interface of intimate contact and improve the conductivity [22]. With this strategy, herein the hierarchical $FeNi_3$@(Fe,Ni)S_2 core–shell heterojunctions with controllable shell thickness were constructed via the reduction of $NiFe(OH)_x$ nanosheets followed by a partial

Address correspondence to Zheng Hu, zhenghu@nju.edu.cn; Lijun Yang, lijunyang@nju.edu.cn

sulfidization. The conductive $FeNi_3$ core provides the highway for electron transport, and the Ni-Fe sulfide shell offers exposed surface for *in situ* generation of S-doped NiFe-oxyhydroxides as the OER active species. The optimized catalyst achieves an excellent OER performance with a low overpotential (288 mV at 100 mA·cm^{-2}), small Tafel slope (48 mV·dec^{-1}), and high stability. The significant contributions of the conductive core and the surface S-doped NiFe-oxyhydroxides to the OER performance were revealed by evaluating the evolution of the OER performance with the $(Fe,Ni)S_2$ shell thickness in combination with the theoretical calculation. This study provides an effective way to explore the advanced earth-abundant OER electrocatalysts by constructing the heterojunctions of metal/metal-compounds via the convenient post treatment, such as nitridation and sulfidization.

2 Experimental

2.1 Synthesis

Preparation of $NiFe(OH)_x$ nanosheets: The sphere-like hierarchical $NiFe(OH)_x$ precursors were prepared by hydrothermal method. Specifically, $Ni(NO_3)_3{\cdot}6H_2O$ (3 mmol), $Fe(NO_3)_3{\cdot}9H_2O$ (1 mmol), urea (20 mmol), NH_4F (10 mmol), and oxalic acid (0.8 mmol) were dissolved to form a solution (70 mL). Then the solution was poured into 100 mL Teflon-lined stainless-steel autoclave, and heated at 120 °C for 6 h. The yellow precipitate was formed and rinsed by deionized water and ethanol several times, and then dried at 60 °C for 12 h.

Preparation of $FeNi_3$ alloy: The $FeNi_3$ alloy was prepared by an *in situ* reduction process of the $NiFe(OH)_x$ nanosheets precursor. Specifically, the as-prepared $NiFe(OH)_x$ nanosheets were reduced in H_2/Ar (10/90, v/v) stream at 250 °C for 2 h. The reduction process leads to the chemical transformation from $NiFe(OH)_x$ nanosheets to $FeNi_3$ alloy nanoparticles. The resulting product was slowly cooled to room temperature for the subsequent use.

Preparation of $FeNi_3$@$(Fe,Ni)S_2$ core–shell heterojunctions and pure $(Fe,Ni)S_2$: To prepare $FeNi_3$@$(Fe,Ni)S_2$ core–shell heterojunctions, 20 mg $FeNi_3$ alloy and appropriate amount of sulfur powder were placed in two ends of a porcelain boat, with the sulfur powder on the upstream side of the furnace. The samples were heated to 300 °C with a heating rate of 2 °C min^{-1} in Ar atmosphere and kept there for 2 h, then cooled down to room temperature naturally, and the $FeNi_3$@$(Fe,Ni)S_2$ was thus obtained. The ratio of $FeNi_3$ to $(Fe,Ni)S_2$ were regulated by using different sulfur amount of 10, 20, and 30 mg, respectively, while keeping the $FeNi_3$ amount constant. The corresponding $FeNi_3$@$(Fe,Ni)S_2$ samples were designated as $FeNi_3$@$(Fe,Ni)S_2$-n (n = 3.6, 7.2, and 10.8), where n corresponds to the molar ratio of sulfur powder to $FeNi_3$. The pure $(Fe,Ni)S_2$ sample was prepared similarly except for more sulfur powder (40 mg) and longer sulfidation time (12 h).

2.2 Characterizations

The morphologies, structures, and composition of the samples were characterized by scanning electron microscope (SEM, Hitachi, S-4800), high resolution transmission electron microscopy (HRTEM, JEM-2100) and X-ray diffraction (XRD) with a Bruker D8 diffractometer using a Co Kα radiation. X-ray absorption fine structure (XAFS) spectra were recorded on BL14W1 beamline of Shanghai Synchrotron Radiation Facility and analyzed with IFEFFIT software. Nitrogen adsorption–desorption isotherms were conducted using a Thermo Fisher scientific surface gas adsorption porosimeter at 77 K. Prior to the measurement, the catalyst powders were degassed at 100 °C for 6 h. The specific surface area is calculated by using the Brunauer–Emmett–Teller (BET) equation. The conductivity was measured by a four-probe method using a source measure unit (SUM, Keithley 6430). The surface species were analyzed by X-ray photoelectron spectroscopy (XPS, VG ESCALAB MKII).

2.3 Electrochemical measurements

The electrochemical measurements were conducted in 1 M KOH solution on Biologic VMP3 electrochemical workstation. The catalyst-loaded Ni foam, Ag/AgCl electrode (3 M KCl), and carbon rod were used as the working, reference, and counter electrode, respectively. The working electrode was prepared by coating the slurry of catalyst and polyvinylidene fluoride (PVDF) (with the mass ratio of 9:1) onto the Ni foam with the geometric area (A) of ca. 0.8 cm^{-2} and mass loading of ca. 1.25 mg·cm^{-2}, followed by drying at 100 °C for 12 h. The polarization curves for OER were obtained by linear sweep voltammetry in the potential window of 0–0.8 V (vs. Ag/AgCl) at a scan rate of 5 mV·s^{-1}. The potentials were iR corrected and converted to referring to the reversible hydrogen electrode (RHE) according to the Nernst equation ($E_{RHE} = E_{Ag/AgCl} + 0.0591 \times pH + 0.209$). The electrochemical impedance spectroscopy (EIS) tests were conducted within the frequency range of 100 kHz–0.01 Hz. The long-term durability test was carried out by chronopotentiometric (CP) measurement without compensating *iR* drop.

The values of the mass activity (MA, A·g^{-1}) for the samples were calculated from the catalysts loading (m = 1.25 mg·cm^{-2}) and the measured current density j (mA·cm^{-2}) at the overpotential of 300 mV by the following equation [26]:

$$MA = j/m \quad (1)$$

The electrochemically active surface area (ECSA) of the catalyst was calculated by measuring the double-layer capacitance (C_{dl}) with 0.1 V potential window. The ECSA was obtained according to the following equation [27]:

$$ECSA = A \times C_{dl}/C_s \quad (2)$$

where A is the geometric area, ca. 0.8 cm^{-2}; C_s is the specific capacitance of atomically smooth planar per unit area with the value of 40 μF·cm^{-2} for non-precious metals.

The specific activity (SA, mA·cm^{-2}) was calculated by [28, 29]:

$$SA = A \times j/ECSA \quad (3)$$

The TOF was quantified by the concentration of active site and calculated by [30, 31]:

$$TOF = A \times j/4FM \quad (4)$$

where 4 is the electron transfer number for OER; F is the Faradic constant (96,485 C·mol^{-1}); M is the number of active sites (mol), which can be extracted from the linear relationship between the oxidation peak currents and scan rate by the following equation [30]:

$$Slope = n^2F^2M/4RT \quad (5)$$

where n (1) is the number of electron transfer for the redox reaction; R and T are the ideal gas constant and the absolute temperature, respectively.

2.4 Theoretical calculations

The DMol3 8.0 was employed to perform all the spin-polarized density functional theory (DFT) calculations within the generalized gradient approximation (GGA) using the Perdew–Burke–Ernzerhof (PBE) formulation [32–34]. A Fermi smearing

of 5.0 × 10^{-3} Ha (1 Ha = 27.211 eV) was used to accelerate convergence. We used the DFT semi-core pseudopotentials to describe the core electrons and took valence electrons into account using a double numerical basis set including p-polarization function (DNP) with the orbital cutoff of 4.7 Å. The electronic energy was considered self-consistent when the energy change was smaller than 10^{-6} eV. A geometry optimization was considered convergent when the energy change was smaller than 10^{-5} eV. Dispersion corrected DFT (DFT-D) scheme was used to describe the dispersion interactions among all the atoms in adsorption models of interest [35].

For bandgap calculations, the CASTEP was used to perform all the spin-polarized DFT within the GGA using the PBE formulation [34]. The cutoff energy for the plane wave basis set was set to 300 eV. All the calculations were performed with a 3 × 3 × 1 Monkhorst-Pack k-point grid.

3 Results and discussion

The construction of core–shell heterojunctions of $FeNi_3$@$(Fe,Ni)S_2$ is schemed in Fig. 1. The fabrication was achieved by the sequential steps, i.e., the hydrothermal reaction to obtain the $NiFe(OH)_x$ (step (I)), followed by the thermal reduction to $FeNi_3$ (step (II)), and the partial sulfidization to core–shell $FeNi_3$@$(Fe,Ni)S_2$ (step (III)) or the complete sulfidization to $(Fe,Ni)S_2$ (step (IV)). During the OER, the *in situ* formed surface S-doped NiFe-oxyhydroxides catalyze the OER process (step (V)).

Figure 2 shows the morphological evolution in preparation of the core–shell $FeNi_3$@$(Fe,Ni)S_2$ and the structural characterization on the typical sample of $FeNi_3$@$(Fe,Ni)S_2$-7.2. During the sequential transformation from $NiFe(OH)_x$ to $FeNi_3$, $FeNi_3$@$(Fe,Ni)S_2$ and $(Fe,Ni)S_2$ (steps (I) to (IV) in Fig. 1), the sample maintains the spherical porous hierarchical architectures (Figs. 2(a)–2(d)), while the components change from the sheet-like for $NiFe(OH)_x$ to the particle-like for the rests (Figs. 2(a_1)–(d_1)). The TEM image of the typical particle taken from $FeNi_3$@$(Fe,Ni)S_2$-7.2 in Fig. 2(c) exhibits the core–shell structure with a shell thickness of ca. 17 nm and core diameter of ca. 70 nm, as learnt from the different contrast (Fig. 2(e)). This architecture was confirmed by the corresponding energy dispersive X-ray spectroscopic (EDS) line-scan profile across this nanoparticle, which shows the stronger EDS signals for S at the edges than at the center, whereas much stronger counts for Ni and Fe at the center than at the edges (Fig. 2(f)). The $FeNi_3$@$(Fe,Ni)S_2$ core–shell structure is also supported by the XRD, elemental mapping, and XAFS (Figs. S1–S3 in the Electronic Supplementary Material (ESM)). The lattice-matching of $FeNi_3$(200)/$(Fe,Ni)S_2$(200) at the interface was observed in the HRTEM image. The (200) planes of $(Fe,Ni)S_2$ elongate across the interface and twist a certain angle for releasing strain to match the (200) planes of $FeNi_3$, as clearly shown in the inverse fast Fourier transformation (FFT) images (Figs. 2(g) and 2(h)). The XPS characterization shows that the binding energy of S 2p for the $FeNi_3$@$(Fe,Ni)S_2$-7.2 has an obvious negative shift compared with that of the control sample of $(Fe,Ni)S_2$, indicating the electrons transfer from the $FeNi_3$ core to the $(Fe,Ni)S_2$ shell (Fig. 2(i)). This result is supported by the charge differential calculation (Fig. S4 in the ESM). As expected, the binding energies of Ni 2p and Fe 2p for the $FeNi_3$@$(Fe,Ni)S_2$-7.2 are in between the corresponding ones for the control samples of $FeNi_3$ and $(Fe,Ni)S_2$ (Fig. S5 and Table S1 in the ESM). The $FeNi_3$@$(Fe,Ni)S_2$-7.2 shows a high conductivity of 525 S·m^{-1}, much higher than 103 S·m^{-1} for the control sample of $(Fe,Ni)S_2$, and only slightly lower than 579 S·m^{-1} for $FeNi_3$ (Fig. S6 in the ESM). Meanwhile, it possesses a large specific surface area of 75.8 m^2·g^{-1}, much larger than those of the Ni-Fe sulfides in literatures (Fig. S7 in the ESM) [36, 37].

The preceding results indicate the $FeNi_3$@$(Fe,Ni)S_2$ core–shell structure was constructed with the atomic epitaxy at the interface of $FeNi_3$ core and $(Fe,Ni)S_2$ shell. With this configuration, the high conductivity ensured by the $FeNi_3$ core could facilitate the electron transfer and the *in situ* generated NiFe-oxyhydroxides during OER favors the intermediates adsorption. The large surface area could provide more active sites and the porous hierarchical structure could promote the electrolyte ion diffusion and O_2 liberation. These merits synergistically boost the OER activity.

As known, the core–shell $FeNi_3$@$(Fe,Ni)S_2$ samples are actually the pre-catalysts and the surface metal oxyhydroxides *in situ* generated upon applying the potential are the real active species for the OER [14, 15]. Hence, the suitable thickness of the $(Fe,Ni)S_2$ shell is a critical parameter governing the OER performance, since a too thick shell would hinder the electron tunneling while a too thin shell cannot generate enough metal oxyhydroxide active species. The thickness could be tuned by changing the S:$FeNi_3$ ratio from 3.6 to 7.2 and 10.8 in preparation (experimental section). In comparison with the single-phase counterparts of $FeNi_3$, $(Fe,Ni)S_2$, and the benchmark of RuO_2, generally the core–shell $FeNi_3$@$(Fe,Ni)S_2$ samples exhibit higher activity with lower overpotential and faster OER kinetics, as shown in Fig. 3 (Fig. S8 in the ESM). The optimized $FeNi_3$@$(Fe,Ni)S_2$-7.2 sample with the medium shell thickness exhibits the highest OER activity with the lowest overpotential of 288 mV at 100 mA·cm^{-2}, which is much lower than those of $FeNi_3$ (334 mV at 100 mA·cm^{-2}) and $(Fe,Ni)S_2$ (313 mV at 100 mA·cm^{-2}). The Ni foam serves as the support with little contribution to the OER activity (Fig. 3(a)). The OER kinetics of the catalysts were evaluated by Tafel slope and EIS [40, 41]. The Tafel slope of $FeNi_3$@$(Fe,Ni)S_2$-7.2 (48 mV·dec^{-1}) is much smaller than those of $FeNi_3$ (70 mV·dec^{-1}) and $(Fe,Ni)S_2$ (99 mV·dec^{-1}) (Fig. 3(b)). In addition, the $FeNi_3$@$(Fe,Ni)S_2$-7.2 has the smallest charge-transfer resistance (R_{ct}), indicating the best charge transfer kinetics (Fig. S9 in the ESM). The small Tafel slope and R_{ct} ensure the fast OER kinetics for the $FeNi_3$@$(Fe,Ni)S_2$-7.2. The intrinsic activities of the catalysts were estimated by the turn over frequency (TOF) and specific activity [42–44]. The TOF and specific activity of

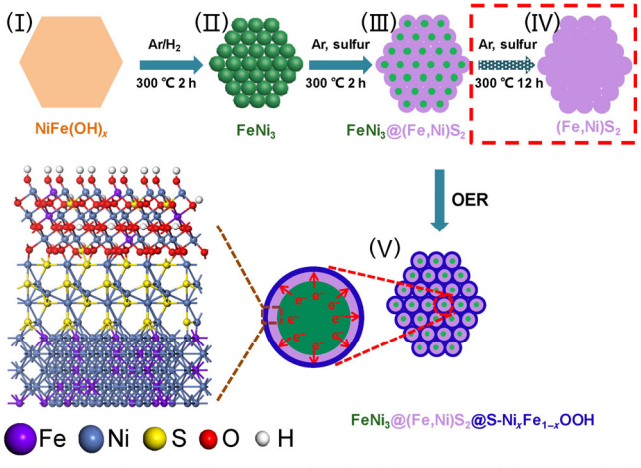

Figure 1 Schematic illustration for the fabrication of the core–shell $FeNi_3$@$(Fe,Ni)S_2$ and the *in situ* generation of S-$Ni_xFe_{1-x}OOH$. (I) $NiFe(OH)_x$, (II) $FeNi_3$, (III) the core–shell $FeNi_3$@$(Fe,Ni)S_2$, (IV) $(Fe,Ni)S_2$, and (V) *In situ* generation of S-$Ni_xFe_{1-x}OOH$ during the OER. Note: The local magnification in (V) is the theoretical model of the $FeNi_3$@$(Fe,Ni)S_2$@S-$Ni_xFe_{1-x}OOH$.

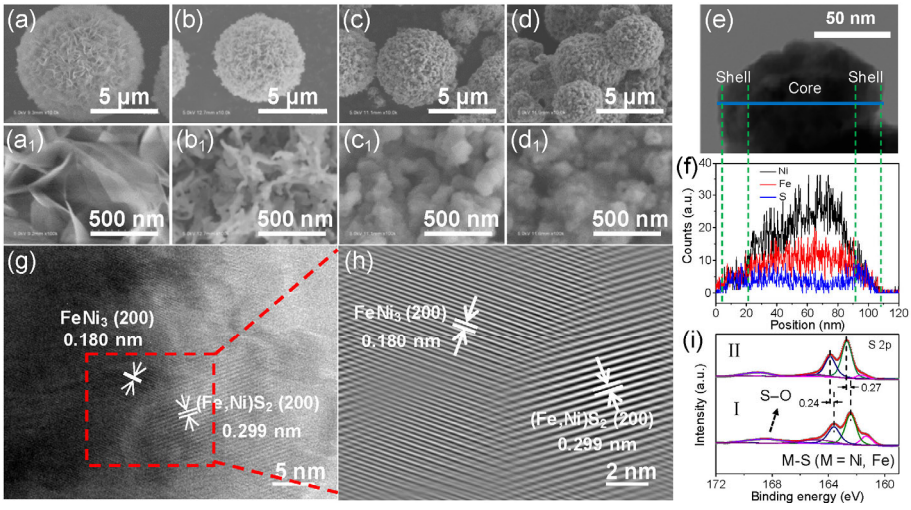

Figure 2 The morphological evolution for preparing the core–shell $FeNi_3$@(Fe,Ni)S_2-7.2 and corresponding structural characterizations. ((a)–(d) and (a_1)–(d_1)) SEM images of $NiFe(OH)_x$ ((a) and (a_1)), $FeNi_3$ ((b) and (b_1)), $FeNi_3$@(Fe,Ni)S_2-7.2 ((c) and (c_1)), and (Fe,Ni)S_2 ((d) and (d_1)). (e) and (f) TEM image of a typical core–shell nanoparticle from (c) and corresponding EDS line scan profile. (g) and (h): HRTEM image (g) and corresponding inverse FFT image (h) at the core–shell interface for the nanoparticle in (e). (i) The S 2p XPS spectra for the $FeNi_3$@(Fe,Ni)S_2-7.2 (I) and the control sample of (Fe,Ni)S_2 (II).

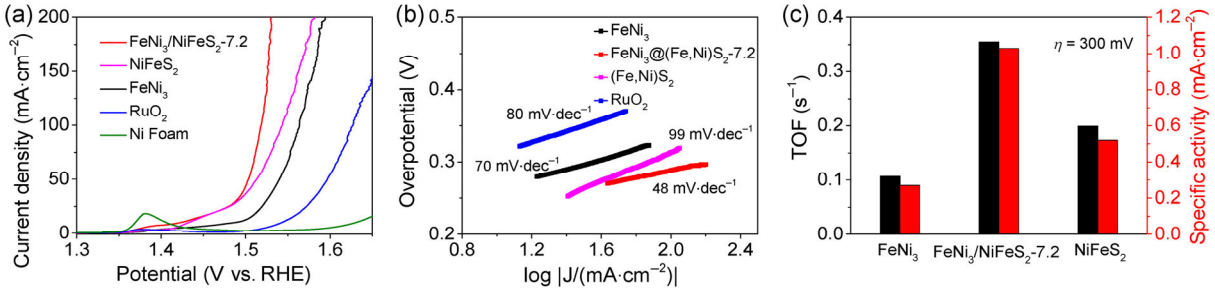

Figure 3 The OER performances of the $FeNi_3$@(Fe,Ni)S_2-7.2, $FeNi_3$ and (Fe,Ni)S_2 samples. (a,b) The polarization curves (a) and corresponding Tafel plots (b). (c) TOF and specific activity at an overpotential of 300 mV. Note: The data for Ni foam and RuO_2 in (a) and (b) are presented for comparison [38, 39].

$FeNi_3$@(Fe,Ni)S_2-7.2 are ca. 0.355 s^{-1} and 1.03 $mA·cm^{-2}$, respectively, much higher than the corresponding 0.107 s^{-1} and 0.27 $mA·cm^{-2}$ for $FeNi_3$, and 0.199 s^{-1} and 0.52 $mA·cm^{-2}$ for (Fe,Ni)S_2 (Fig. 3(c), and Figs. S10 and S11 in the ESM). The mass activity of $FeNi_3$@(Fe,Ni)S_2-7.2 at the overpotential of 300 mV is ca. 151 $A·g^{-1}$, much higher than those of the $FeNi_3$ (29 $A·g^{-1}$) and (Fe,Ni)S_2 (60 $A·g^{-1}$) (Fig. S12 in the ESM). Hence, the optimized $FeNi_3$@(Fe,Ni)S_2-7.2 shows an excellent OER performance for the non-precious metal electrocatalysts (Tables S2 and S3, and Fig. S13 in the ESM).

The OER stability of the optimized $FeNi_3$@(Fe,Ni)S_2-7.2 was measured by CP and the corresponding structural evolution was monitored by XRD and XPS (Fig. 4). In the constant–current CP curve with a low current density of 20 $mA·cm^{-2}$, the $FeNi_3$@(Fe,Ni)S_2-7.2 demonstrates an excellent stability with a negligible potential increase of ca. 8 mV after 50 h test (Fig. 4(a)). In the multistep CP curve with the increment of 20 $mA·cm^{-2}$ per hour, the potential slightly increases for the first step and then remains almost unchanged for the rest steps. The slight potential increase for the first step comes from the formation of the surface metal oxyhydroxides. The unchanged potential for the rest steps means the quick respond to the change of current density, indicating the high electrical conductivity of the material and the rapid inward diffusion of OH^- and outwards diffusion of oxygen bubbles (Fig. 4(b)) [22, 45, 46]. Even at a high current density of 200 $mA·cm^{-2}$, the $FeNi_3$@(Fe,Ni)S_2-7.2 still exhibits a ultrastability during 1,200 h test (Fig. S14 in the ESM).

XRD results show that the (Fe,Ni)S_2 phase in $FeNi_3$@(Fe,Ni)S_2-7.2 disappeared after 10 h operation due to the transformation of the (Fe,Ni)S_2 shell into the metal oxyhydroxides during the OER (Fig. S15 in the ESM), which is supported by the XPS analysis. In the Ni 2p and Fe 2p spectra, the intensities (or the areas) of the minor peaks from M^0 (M = Ni and Fe) components decrease while the major peak mainly from M^{2+} species shift positively owing to the formation of metal oxyhydroxides (Figs. 4(c) and 4(d)). This evolution is also supported by the O1s spectra, in which the position of the peak II (–OH signal at ~ 531.5 eV) has a slight negative shift [47] and the areal ratio of peak II to peak I (the lattice oxygen at ~ 529.8 eV) increases from 4.6 to 6.5 due to the transformation from the (Fe,Ni)S_2 shell to NiFe-oxyhydroxides (Fig. 4(e)) [22]. Meanwhile, the intensity of sulfur greatly decreased after the OER, indicating the partial loss during the transformation (Fig. 4(f)). It is noted that the intensity ratio for S–O species to S-Ni and S-Fe species is much enhanced after the 10 h OER in comparison with the case for the pristine sample, suggesting the formation of S-doped $Ni_xFe_{1-x}OOH$. The corresponding catalyst maintained the good structural integrity with an amorphous S-$Ni_xFe_{1-x}OOH$ layer formed on the surface (Fig. S16 in the ESM). Hence, the *in situ* generated S-doped oxyhydroxide species on the catalyst surface at the expense of the (Fe,Ni)S_2 shell should be the active species for OER. The coating of the S-$Ni_xFe_{1-x}OOH$ prevents further oxidation of the $FeNi_3$@(Fe,Ni)S_2-7.2 catalyst, guaranteeing the ultrahigh stability (Fig. S14 in the ESM) [48].

The effect of S doping on OER activity was further studied by the DFT modeling. The model of S-$Ni_xFe_{1-x}OOH$ was chosen as the active species to calculate the free-energy diagram. The reaction steps of OER were referenced from the previous

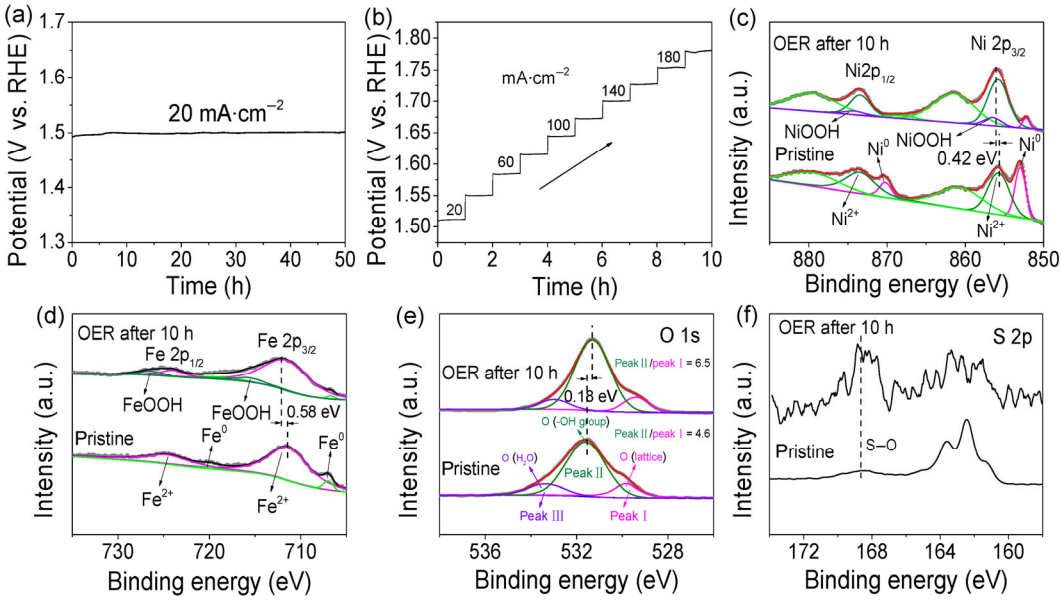

Figure 4 The OER stability of the optimized $FeNi_3$@(Fe,Ni)S_2-7.2 and corresponding structural evolution. (a) CP curve at a constant current density of 20 mA·cm^{-2}. (b) Multistep CP curve with the increment of 20 mA·cm^{-2} per hour in the current density range of 20–200 mA·cm^{-2}. (c)–(f) Evolutions of XPS spectra of Ni 2p (c), Fe 2p (d), O 1s (e), and S 2p (f).

study on (Ni,Fe)OOH by W. A. Goddard [16]. With this setup, the calculated thermodynamic theoretical overpotential (η) of OER follows the order of S-$Ni_xFe_{1-x}OOH$ < $Ni_xFe_{1-x}OOH$ < NiOOH, indicating the enhancement of the intrinsic OER activity upon the introduction of S dopant. Meanwhile, S-doping improves the conductivity of NiFe-oxyhydroxides, as reflected in the smaller bandgap of S-$Ni_xFe_{1-x}OOH$ than $Ni_xFe_{1-x}OOH$, which is also a favorable factor for the enhancement of OER activity (Fig. S17 in the ESM).

In our recent study, by nitriding the NiFe-based precursors, the porous hierarchical ($Ni_{3-x}Fe_x$)FeN/Ni heterojunctions were prepared and exhibited excellent OER performance [22]. In this study, the $FeNi_3$@(Fe,Ni)S_2 core–shell heterojunctions were successfully constructed by the partial sulfidization of the pre-formed porous $FeNi_3$ alloy particles, which also showed superior OER activity. These results indicate the general validity can enhance the OER activity by constructing the heterojunctions between metal and corresponding metal-compounds via the convenient post treatment, such as nitridation, sulfidization, phosphorization, or oxidization (Fig. S18 in the ESM), which provides an effective way to explore the advanced earth-abundant OER electrocatalysts.

4 Conclusions

In summary, the porous hierarchical $FeNi_3$@(Fe,Ni)S_2 core–shell heterojunctions were successfully constructed by the reduction of $NiFe(OH)_x$ nanosheets followed by the convenient post treatment of controllable sulfidization. The unique structure and morphology as well as the interaction between the core and shell were well characterized by different means including SEM, HRTEM, XRD, XPS, EDS, EXAFS, and so on. The conductive scaffold of $FeNi_3$ core significantly enhances the conductivity and provides the highway for electron transport, and the (Fe,Ni)S_2 shell offers the exposed surface for *in situ* generation of S-doped NiFe-oxyhydroxides with high intrinsic OER activity, which was demonstrated by the combined experimental and theoretical studies. In addition, the porous hierarchical morphology favors the electrolyte access and O_2 gas release. Benefiting from these merits, the optimized $FeNi_3$@(Fe,Ni)S_2-7.2 catalyst exhibited an excellent OER performance, with a low overpotential (288 mV at 100 mA·cm^{-2}), a small Tafel slope (48 mV·dec^{-1}), as well as an ultrahigh stability (1,200 h at 200 mA·cm^{-2}). This study provides an effective way to explore the advanced earth-abundant OER electrocatalysts by constructing the heterojunctions between metal and corresponding metal-compounds via the convenient post treatment, such as nitridation, sulfidization, phosphorization, or oxidization.

Acknowledgements

This work was jointly supported by the National Key Research and Development Program of China (Nos. 2017YFA0206500 and 2018YFA0209103), the National Natural Science Foundation of China (Nos. 52071174, 21832003, 21773111, and 21972061), and the Fundamental Research Funds for the Central Universities (No. 020514380126). The numerical calculations have been done on the computing facilities in the High Performance Computing Center (HPCC) of Nanjing University. We thank the staff of the BL14W1 beamline at Shanghai Synchrotron Radiation Facility for assistance with the X-ray absorption measurements.

Electronic Supplementary Material: Supplementary material (the detailed characterizations, including XRD, EDS, XAFS, conductivity measurements, and N_2 adsorption–desorption isotherms; additional electrochemical results and the performance comparison with the literature) is available in the online version of this article at https://doi.org/10.1007/s12274-021-3531-8.

Reference

[1] Du, P. W.; Eisenberg, R. Catalysts made of earth-abundant elements (Co, Ni, Fe) for water splitting: Recent progress and future challenges. *Energy Environ. Sci.* **2012**, *5*, 6012–6021.

[2] Ismail, M. S.; Moghavvemi, M.; Mahlia, T. M. I.; Muttaqi, K. M.; Moghavvemi, S. Effective utilization of excess energy in standalone hybrid renewable energy systems for improving comfort ability and reducing cost of energy: A review and analysis. *Renew. Sust. Energ. Rev.* **2015**, *42*, 726–734.

[3] Liu, Y. K.; Jiang, S.; Li, S. J.; Zhou, L.; Li, Z. H.; Li, J. M.; Shao,

M. F. Interface engineering of (Ni, Fe)S_2@MoS_2 heterostructures for synergetic electrochemical water splitting. *Appl. Catal. B: Environ.* **2019**, *247*, 107–114.

[4] Turner, J. A. Sustainable hydrogen production. *Science* **2004**, *305*, 972–974.

[5] Gong, M.; Dai, H. J. A mini review of NiFe-based materials as highly active oxygen evolution reaction electrocatalysts. *Nano Res.* **2015**, *8*, 23–39.

[6] Zhou, D. J.; Wang, S. Y.; Jia, Y.; Xiong, X. Y.; Yang, H. B.; Liu, S.; Tang, J. L.; Zhang, J. M.; Liu, D.; Zheng, L. R. et al. NiFe hydroxide lattice tensile strain: Enhancement of adsorption of oxygenated intermediates for efficient water oxidation catalysis. *Angew. Chem., Int. Ed.* **2019**, *58*, 736–740.

[7] Wang, Y. Q.; Chen, S.; Zhang, J. T. Hierarchical assembly of prussian blue derivatives for superior oxygen evolution reaction. *Adv. Funct. Mater.* **2019**, *29*, 1904955.

[8] Peng, X.; Yan, Y. J.; Jin, X.; Huang, C.; Jin, W. H.; Gao, B.; Chu, P. K. Recent advance and prospectives of electrocatalysts based on transition metal selenides for efficient water splitting. *Nano Energy* **2020**, *78*, 105234.

[9] Yang, M. Q.; Wang, J.; Wu, H.; Ho, G. W. Noble metal-free nanocatalysts with vacancies for electrochemical water splitting. *Small* **2018**, *14*, 1703323.

[10] Yan, Y.; Xia, B. Y.; Zhao, B.; Wang, X. A review on noble-metal-free bifunctional heterogeneous catalysts for overall electrochemical water splitting. *J. Mater. Chem. A* **2016**, *4*, 17587–17603.

[11] Wang, Y. Q.; Ma, J. Z.; Wang, J.; Chen, S.; Wang, H. S.; Zhang, J. T. Interfacial scaffolding preparation of hierarchical PBA-based derivative electrocatalysts for efficient water splitting. *Adv. Energy Mater.* **2019**, *9*, 1802939.

[12] Guo, D. Y.; Qi, J.; Zhang, W.; Cao, R. Surface electrochemical modification of a nickel substrate to prepare a NiFe-based electrode for water oxidation. *ChemSusChem* **2017**, *10*, 394–400.

[13] Edison, T. A. Electrolyte for alkaline storage batteries. U.S. Patent 0,876,445, Jan. 14, 1908.

[14] Duan, Y.; Yu, Z. Y.; Hu, S. J.; Zheng, X. S.; Zhang, C. T.; Ding, H. H.; Hu, B. C.; Fu, Q. Q.; Yu, Z. L.; Zheng, X. et al. Scaled-up synthesis of amorphous NiFeMo oxides and their rapid surface reconstruction for superior oxygen evolution catalysis. *Angew. Chem., Int. Ed.* **2019**, *58*, 15772–15777.

[15] Zhang, J. F.; Liu, J. Y.; Xi, L. F.; Yu, Y. F.; Chen, N.; Sun, S. H.; Wang, W. C.; Lange, K. M.; Zhang, B. Single-atom Au/NiFe layered double hydroxide electrocatalyst: Probing the origin of activity for oxygen evolution reaction. *J. Am. Chem. Soc.* **2018**, *140*, 3876–3879.

[16] Xiao, H.; Shin, H.; Goddard III, W. A. Synergy between Fe and Ni in the optimal performance of (Ni,Fe)OOH catalysts for the oxygen evolution reaction. *Proc. Natl. Acad. Sci. USA* **2018**, *115*, 5872–5877.

[17] Saad, A.; Shen, H. J.; Cheng, Z. X.; Arbi, R.; Guo, B. B.; Hui, L. S.; Liang, K. Y.; Liu, S. Q.; Attfield, J. P.; Turak, A. et al. Mesoporous ternary nitrides of earth-abundant metals as oxygen evolution electrocatalyst. *Nano-Micro Lett.* **2020**, *12*, 79.

[18] Yin, X. C.; Sun, G.; Wang, L. X.; Bai, L.; Su, L.; Wang, Y. Z.; Du, Q. H.; Shao, G. J. 3D hierarchical network $NiCo_2S_4$ nanoflakes grown on Ni foam as efficient bifunctional electrocatalysts for both hydrogen and oxygen evolution reaction in alkaline solution. *Int. J. Hydrogen Energy* **2017**, *42*, 25267–25276.

[19] Lv, J. J.; Wu, S. J.; Qiao, M.; Li, L. L.; Zhu, J. J. Mesoporous $NiCoP_x$ nanoplates as highly efficient electrocatalysts for overall water splitting. *J. Power Sources* **2018**, *400*, 434–440.

[20] Li, J. W.; Song, J. D.; Huang, B. Y.; Liang, G. F.; Liang, W. L.; Huang, G. J.; Qi Jin, Y.; Zhang, H.; Xie, F. Y.; Chen, J. et al. Enhancing the oxygen evolution reaction performance of NiFeOOH electrocatalyst for Zn-air battery by N-doping. *J. Catal.* **2020**, *389*, 375–381.

[21] Niu, S.; Jiang, W. J.; Wei, Z. X.; Tang, T.; Ma, J. M.; Hu, J. S.; Wan, L. J. Se-doping activates FeOOH for cost-effective and efficient electrochemical water oxidation. *J. Am. Chem. Soc.* **2019**, *141*, 7005–7013.

[22] Yan, M. L.; Mao, K.; Cui, P. X.; Chen, C.; Zhao, J.; Wang, X. Z.; Yang, L. J.; Yang, H.; Wu, Q.; Hu, Z. *In situ* construction of porous hierarchical ($Ni_{3-x}Fe_x$)FeN/Ni heterojunctions toward efficient electrocatalytic oxygen evolution. *Nano Res.* **2020**, *13*, 328–334.

[23] Liang, H. F.; Gandi, A. N.; Xia, C.; Hedhili, M. N.; Anjum, D. H.; Schwingenschlögl, U.; Alshareef, H. N. Amorphous NiFe-OH/NiFeP electrocatalyst fabricated at low temperature for water oxidation applications. *ACS Energy Lett.* **2017**, *2*, 1035–1042.

[24] Mahala, C.; Sharma, M. D.; Basu, M. 2D nanostructures of $CoFe_2O_4$ and $NiFe_2O_4$: Efficient oxygen evolution catalyst. *Electrochim. Acta* **2018**, *273*, 462–473.

[25] Peng, X.; Wang, L.; Hu, L. S.; Li, Y.; Gao, B.; Song, H.; Huang, C.; Zhang, X. M.; Fu, J. J.; Huo, K. F. et al. *In situ* segregation of cobalt nanoparticles on VN nanosheets via nitriding of $Co_2V_2O_7$ nanosheets as efficient oxygen evolution reaction electrocatalysts. *Nano Energy* **2017**, *34*, 1–7.

[26] Sun, F. Z.; Wang, G.; Ding, Y. Q.; Wang, C.; Yuan, B. B.; Lin, Y. Q. NiFe-based metal-organic framework nanosheets directly supported on nickel foam acting as robust electrodes for electrochemical oxygen evolution reaction. *Adv. Energy Mater.* **2018**, *8*, 1800584.

[27] Yu, X. W.; Zhang, M.; Tong, Y.; Li, C.; Shi, G. Q. A large-scale graphene-bimetal film electrode with an ultrahigh mass catalytic activity for durable water splitting. *Adv. Energy Mater.* **2018**, *8*, 1800403.

[28] Tao, L.; Qiao, M.; Jin, R.; Li, Y.; Xiao, Z. H.; Wang, Y. Q.; Zhang, N. N.; Xie, C.; He, Q. G.; Jiang, D. C. et al. Bridging the surface charge and catalytic activity of a defective carbon electrocatalyst. *Angew. Chem., Int. Ed.* **2019**, *58*, 1019–1024.

[29] Yang, J. L.; Xiao, Y. G.; Zhao, Q. H.; Zhang, G. X.; Wang, R.; Teng, G. G.; Chen, X.; Weng, M.; He, D.; Mu, S. et al. Synergistic effect of charge transfer and short H-bonding on nanocatalyst surface for efficient oxygen evolution reaction. *Nano Energy* **2019**, *59*, 443–452.

[30] Wu, D.; Wei, Y. C.; Ren, X.; Ji, X. Q.; Liu, Y. W.; Guo, X. D.; Liu, Z. A.; Asiri, A. M.; Wei, Q.; Sun, X. P. $Co(OH)_2$ nanoparticle-encapsulating conductive nanowires array: Room-temperature electrochemical preparation for high-performance water oxidation electrocatalysis. *Adv. Mater.* **2018**, *30*, 1705366.

[31] Pintado, S.; Goberna-Ferrón, S.; Escudero-Adán, E. C.; Galán-Mascarós, J. R. Fast and persistent electrocatalytic water oxidation by Co-Fe prussian blue coordination polymers. *J. Am. Chem. Soc.* **2013**, *135*, 13270–13273.

[32] Delley, B. An all-electron numerical method for solving the local density functional for polyatomic molecules. *J. Chem. Phys.* **1990**, *92*, 508–517.

[33] Delley, B. From molecules to solids with the $DMol^3$ approach. *J. Chem. Phys.* **2000**, *113*, 7756–7764.

[34] Perdew, J. P.; Burke, K.; Ernzerhof, M. Generalized gradient approximation made simple. *Phys. Rev. Lett.* **1996**, *77*, 3865.

[35] Grimme, S.; Antony, J.; Ehrlich, S.; Krieg, H. A consistent and accurate *ab initio* parametrization of density functional dispersion correction (DFT-D) for the 94 elements H-Pu. *J. Chem. Phys.* **2010**, *132*, 154104.

[36] Che, Q. J.; Li, Q.; Tan, Y.; Chen, X. H.; Xu, X.; Chen, Y. S. One-step controllable synthesis of amorphous (Ni-Fe)S_x/NiFe(OH)$_y$ hollow microtube/sphere films as superior bifunctional electrocatalysts for quasi-industrial water splitting at large-current-density. *Appl. Catal. B: Environ.* **2019**, *246*, 337–348.

[37] Wei, P. K.; Li, X. M.; Li, J.; Bai, J. W.; Jiang, C. J.; Liu, L. A facile synthesis of ternary nickel iron sulfide nanospheres as counter electrode in dye-sensitized solar cells. *Chem.—Eur. J.* **2018**, *24*, 19032–19037.

[38] Hao, S. Y.; Chen, L. H.; Yu, C. L.; Yang, B.; Li, Z. J.; Hou, Y.; Lei, L. C.; Zhang, X. W. NiCoMo hydroxide nanosheet arrays synthesized via chloride corrosion for overall water splitting. *ACS Energy Lett.* **2019**, *4*, 952–959.

[39] Wang, B. L.; Zhao, K. N.; Yu, Z.; Sun, C. L.; Wang, Z.; Feng, N. N.; Mai, L. Q.; Wang, Y. G.; Xia, Y. Y. *In situ* structural evolution of the multi-site alloy electrocatalyst to manipulate the intermediate for enhanced water oxidation reaction. *Energy Environ. Sci.* **2020**, *13*, 2200–2208.

[40] Fang, Y. H.; Liu, Z. P. Tafel kinetics of electrocatalytic reactions: From experiment to first-principles. *ACS Catal.* **2014**, *4*, 4364–4376.

[41] Yu, M. Q.; Moon, G.; Bill, E.; Tüysüz, H. Optimizing Ni-Fe oxide electrocatalysts for oxygen evolution reaction by using hard templating as a toolbox. *ACS Appl. Energy Mater.* **2019**, *2*, 1199–1209.

[42] Zhang, J. F.; Hu, Y. C.; Liu, D. L.; Yu, Y.; Zhang, B. Enhancing oxygen evolution reaction at high current densities on amorphous-like Ni-Fe-S ultrathin nanosheets via oxygen incorporation and electrochemical tuning. *Adv. Sci.* **2017**, *4*, 1600343.

[43] Anantharaj, S.; Kundu, S. Do the evaluation parameters reflect intrinsic activity of electrocatalysts in electrochemical water splitting? *ACS Energy Lett.* **2019**, *4*, 1260–1264.

[44] Cai, Z.; Li, L. D.; Zhang, Y. W.; Yang, Z.; Yang, J.; Guo, Y. J.; Guo, L. Amorphous nanocages of Cu-Ni-Fe hydr(oxy)oxide prepared by photocorrosion for highly efficient oxygen evolution. *Angew. Chem., Int. Ed.* **2019**, *58*, 4189–4194.

[45] Lu, X. Y.; Zhao, C. Electrodeposition of hierarchically structured three-dimensional nickel-iron electrodes for efficient oxygen evolution at high current densities. *Nat. Commun.* **2015**, *6*, 6616.

[46] Tang, C.; Cheng, N. Y.; Pu, Z. H.; Xing, W.; Sun, X. P. NiSe nanowire film supported on nickel foam: An efficient and stable 3D bifunctional electrode for full water splitting. *Angew. Chem., Int. Ed.* **2015**, *54*, 9351–9355.

[47] Jiang, J.; Lu, S.; Wang, W. K.; Huang, G. X.; Huang, B. C.; Zhang, F.; Zhang, Y. J.; Yu, H. Q. Ultrahigh electrocatalytic oxygen evolution by iron-nickel sulfide nanosheets/reduced graphene oxide nanohybrids with an optimized autoxidation process. *Nano Energy* **2018**, *43*, 300–309.

[48] Zhou, M.; Weng, Q. H.; Zhang, X. Y.; Wang, X.; Xue, Y. M.; Zeng, X. H.; Bando, Y.; Golberg, D. *In situ* electrochemical formation of core–shell nickel-iron disulfide and oxyhydroxide heterostructured catalysts for a stable oxygen evolution reaction and the associated mechanisms. *J. Mater. Chem. A* **2017**, *5*, 4335–4342.